Electronic and optical properties of GaN/AlN quantum dots on Si(111) subject to in-plane uniaxial stresses and variable excitation

O. Moshe,[1] D. H. Rich,[1,a)] S. Birner,[2] M. Povolotskyi,[3] B. Damilano,[4] and J. Massies[4]
[1]*Department of Physics and The Ilse Katz Institute for Nanoscale Science and Technology, Ben-Gurion University of the Negev, P.O. Box 653, Beer-Sheva 84105, Israel*
[2]*Department of Physics, Walter Schottky Institute, Am Coulombwall 4, 85748 Garching, Germany*
[3]*School of Electrical and Computer Engineering, Purdue University, 207S Martin Jischke Drive, DLR building, Room 441, West Lafayette, Indiana 47906, USA*
[4]*Centre National de la Recherche Scientifique, Centre de Recherche sur l'Hétéro-Epitaxie et ses Applications, Rue B. Gregory, Sophia Antipolis, 06560 Valbonne, France*

(Received 20 July 2010; accepted 14 August 2010; published online 21 October 2010)

We have studied the excitation- and polarization-dependent optical properties of GaN/AlN self-assembled quantum dots (QDs) grown on Si(111) substrates. Ensembles of QDs were subject to various external stress configurations that resulted from the thermal expansion coefficient mismatch between the GaN/AlN layers and the Si(111) substrate and ranged from in-plane uniaxial stress, primarily along the $\langle 11\bar{2}0\rangle$ directions, to in-plane biaxial stress, having magnitudes ranging from 20–30 kbar. Limited regions of uniaxial stress were obtained by exploiting naturally occurring microcracks that form during the postgrowth cooling. These microcracks act as stressors in order to create the highly localized regions of uniaxial stress. The local strain tensors for such QDs, which are subject to an interfacial stress perturbation, have been determined by modeling the dependence of the QD excitonic transition energy on the interfacial stress. Cathodoluminescence (CL) measurements of the excitonic transitions exhibit an in-plane linear polarization anisotropy in close proximity to microcracks. The polarization anisotropy is strongly dependent on the sample temperature and the electron beam excitation conditions used to excite the QD ensemble. Localized CL spectroscopy of the QDs exhibits emissions from both the ground and excited states, whose relative contributions depend on the level of excitation and temperature. Experimental results indicate that the polarization anisotropy vanishes at high temperatures ($\sim$300 K) with an increasing excitation of the QDs, while the anisotropy decreases more slowly with excitation at low temperatures ($\sim$60 K). A theoretical modeling of the effect of carrier filling on the polarization anisotropy and the excitonic transition energy was performed, as based on three-dimensional self-consistent solutions of the Schrödinger and Poisson equations using the 6×6 $\mathbf{k}\cdot\mathbf{p}$ and effective mass methods for calculations of the *e-h* wave functions and electron and hole quasi-Fermi levels for varying levels of state filling. We attribute carrier filling and a thermal excitation of holes into higher energy QD hole states during excitation to account for the observed gradual decrease in the polarization anisotropy with an increasing electron-hole pair excitation density at $T=300$ K.
 [doi:10.1063/1.3490199]

I. INTRODUCTION

In the past decade, much attention has been directed toward GaN/AlN-based wurtzite self-assembled quantum dots (QDs) as a result of potential solid-state light emitting applications in the visible wavelength range.[1–3] An important characteristic of group III-nitride compounds is the existence of a large polarization field, originating from both piezoelectric and pyroelectric polarizations.[4,5] The charge polarization will create electric fields mainly along the [0001] QD growth axis that will be screened in a complex manner when electrons and holes begin to fill the excited energy levels of the QD during sufficient levels of excitation.[5,6] In this work, vertically stacked layers of GaN/AlN self-assembled QDs were grown by the Stranski–Krastanov method on a Si(111) substrate using molecular beam epitaxy (MBE). During the subsequent cooling from growth temperatures, the thermal expansion coefficient mismatch between the Si substrate and GaN/AlN film containing multiple layers of QDs leads to an additional tensile stress at the Si/III-nitride interface, which is partially relaxed by the formation of microcracks that propagate parallel to the interface and along the $\langle 11\bar{2}0\rangle$ directions.[7,8] We have previously demonstrated that these defects serve as excellent stressors which can modify the strain tensor of an ensemble of QDs in close proximity (i.e., within a few microns) of the microcracks and lead to limited regions of in-plane uniaxial stress.[9–11] The excitonic luminescence of QDs with a uniaxial stress perturbation exhibits an in-plane linear polarization anisotropy that depends on temperature.[10–12]

The development of light emitting diodes (LEDs) with linear polarization is a topic of current interest for backlit liquid-crystal displays (LCDs). In LCDs, linearly polarized light is generated within an LCD pixel by passing unpolar-

a)Electronic mail: danrich@bgu.ac.il.

ized light through a polarization filter, followed by a red, green, or blue color filter to create a color pixel source with a desired intensity. During the polarization filtering process ~50% of the light power is absorbed and dissipated as heat. Therefore, by utilizing highly polarized LED sources, a substantial savings in energy may be realized by eliminating need for the polarization filter. Polarized monochromatic light can be generated by InGaN-based LEDs grown on nonpolar orientations.[13,14] Optical intensity modulation of nonpolar InGaN LEDs by an LCD system has been demonstrated.[15] Therefore, a tailoring of the polarization properties of GaN/AlN QD-based light emitters could enable similar applications in LCDs.

In this study, we explore in detail the effects of localized stress perturbations in the GaN/AlN QD system. Using the method of cathodoluminescence (CL) spectroscopy, we excite locally groups or ensembles of vertically stacked QDs. The effects of screening of the polarization field in the QD, state-filling, and changes in the polarization anisotropy with varying excitation were studied both experimentally and theoretically by calculating changes in the electron and hole quasi-Fermi levels. In the calculations, we obtained three-dimensional (3D) self-consistent solutions of the Schrödinger and Poisson equations using the 6×6 $\mathbf{k}\cdot\mathbf{p}$ and effective mass methods for the calculation of the *e-h* wave functions. While previous self-consistent calculations of nitride-based QDs have been reported, primarily theoretical results without extensive experimental measurements were presented in these works.[6,16–18] In this paper, we present and compare our experimental results and theoretical calculations of the QD polarized emission for varying excitation densities and temperatures.

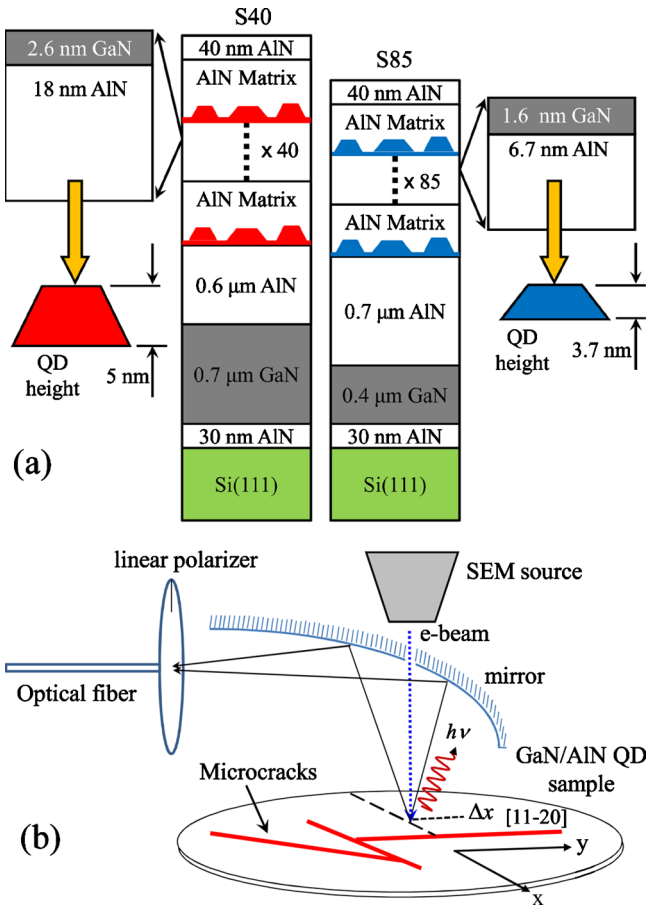

FIG. 1. (Color online) Schematic diagrams of the S40 and S85 wurtzite GaN/AlN QD sample structures in (a) and the geometry for optically detecting polarized CL in (b).

II. EXPERIMENT

The samples were grown by MBE using the two-dimensional (2D) to 3D Stranski–Krastanov growth mode transition.[2,19,20] Two samples were grown on Si(111) substrates and consist of AlN (30 nm)/GaN (400 nm)/AlN (700 nm) buffer layers followed by either 40 or 85 layers of GaN QDs, labeled as samples S40 and S85, respectively. A schematic illustration of the sample structures for S40 and S85 is shown in Fig. 1(a). The growth of sample S40 (S85) involved 18 nm (6.7 nm) thick AlN barrier layers with 2.6 nm (1.6 nm) thick GaN QD layers, resulting in an average dot height of ~5 nm (~3.7 nm), as determined previously by transmission electron microscopy (TEM) measurements for samples possessing very similar structures and growth conditions. The average volumes are also known from TEM and are ~370 nm^3 and ~230 nm^3, respectively, for samples S40 and S85. Both samples were terminated with a 40 nm thick AlN capping layer. The average dot density per QD plane is $\sim5\times10^{11}$ cm^{-2}.

Our CL detection system is mounted on a JEOL 5910 scanning electron microscope (SEM). The samples were mounted on a variable temperature stage that is connected via a copper braid to a closed-cycle He cryorefrigerator. An ellipsoidal mirror with variable three-axis positioning collects luminescence emitted from the sample. The emitted luminescence is collected by the mirror and focused onto a coherent optical fiber bundle with a vacuum rotatable linear polarizer positioned before the fiber optics, as schematically illustrated in Fig. 1(b).[10] Two polarization directions for the polarizer will be denoted with the subscripts $\perp$ and $\parallel$ to indicate detection orientations with **E** perpendicular and parallel to a microcrack that is oriented along the $[11\bar{2}0]$ crystallographic direction. The polarization anisotropy ratio, R_p, is defined by the ratio of the integrated CL intensities, I, under the two orthogonal polarizer orientations and is given by $R_p=I_\perp/I_\parallel$. The light from the flexible fiber bundle was transferred to a 1/4 m monochromator outside the SEM vacuum system. The spectral resolution of the monochromator was 2 nm (~15 meV) at $\lambda=400$ nm (3.100 eV). The dispersed light was detected with a multialkali photomultiplier tube which enabled photon counting. Time-resolved CL experiments were performed with the method of delayed coincidence in an inverted single photon counting mode.[21] Electron beam pulses of 50 ns width with a 1 MHz repetition rate were used to excite the sample.

III. THEORETICAL CALCULATIONS USING A 3D K·P METHOD

The electron and hole wave functions and energies were obtained with 3D 6×6 $\mathbf{k}\cdot\mathbf{p}$ calculations using the NEXTNANO^3 quantum nanostructure simulation code.[9,10,22]

The calculations utilized a 3D Schrödinger equation for wurtzite materials including strain, deformation potentials, spin orbit coupling, and piezoelectric and pyroelectric charges, the latter of which accounts for the large polarization field in the QD along the [0001] growth direction. In order to calculate the wave functions, a single band model for the electrons and a six-band $\mathbf{k}\cdot\mathbf{p}$ Hamiltonian for the holes were employed. The coupling between the conduction and valence bands was neglected, owing to the size of the GaN and AlN bandgaps.[23]

We employed the material parameters used previously for calculations of the polarization field and eigenstates in GaN/AlN QDs.[24–26] The fully strained GaN/AlN QDs were simulated by minimization of the elastic energy within a continuum model approach that takes into account the symmetry of the hexagonal crystal structure. We employed a simulated region size of $19\times19\times22$ nm^3 containing a single pyramidal QD with a typical discretized grid of $60\times70\times112$ nodes for calculations of the strain minimization, Pikus-Bir, $\mathbf{k}\cdot\mathbf{p}$ and single band effective mass Hamiltonians. The geometrical structure parameters for the QD model structures of S40 and S85 were reported previously.[10] External tensile stresses ranging from purely biaxial to uniaxial were used to simulate the thermal stress in the AlN barrier layers in varying proximity to the microcracks.

IV. EXPERIMENTAL RESULTS AND DISCUSSION

A. Excitation-dependent Polarized CL Spectroscopy

The presence of $\langle 11\bar{2}0\rangle$ oriented microcracks in the GaN/AlN/Si samples has been shown to create limited regions of an in-plane uniaxial stress within Δx of ~0.5 to 1.0 μm from the cracks.[9–12] We have previously examined in detail the dependence of R_p ($R_p=I_\perp/I_\parallel$) as a function of distance (Δx) from a microcrack, whose experimental geometry is illustrated in Fig. 1(b). We have shown that R_p decreases monotonically toward $R_p=1$ as the *e*-beam is positioned at distances sufficiently far from the microcracks ($\Delta x > \sim 3$ μm), for various temperatures.[10–12] Again, the maximum value of R_p occurs for the lowest temperature, and this value decreases as the temperature increases. An increased uniaxial tensile stress near the microcrack and an increased biaxial tensile stress far from the microcrack are expected to occur as the temperature is reduced leading to an increased value of the polarization anisotropy at lower temperatures. The polarization anisotropy ratio R_p is a direct probe of deviations from biaxial symmetry.[10,12]

We have performed excitation-dependent local CL spectroscopy measurements by positioning the *e*-beam a distance Δx on a line along a direction perpendicular to a $[11\bar{2}0]$-oriented microcrack, as shown in Fig. 1(b). Stack plots of local CL spectra for sample S85 and S40 are shown in Figs. 2 and 3 for temperatures (T) of 300 K and 60 K, for *e*-beam currents (I_b) ranging from 0.05 to 27 nA, and for positions, Δx, of 0.5 μm and 5 μm, which represent regions of nearly pure uniaxial and biaxial tensile stresses, respectively, as labeled in the panels of Figs. 2 and 3. For regions of uniaxial stress ($\Delta x=0.5$ μm) in S85, Fig. 2 shows that the maximum value of R_p increases from ~1.5 to 2.1 as

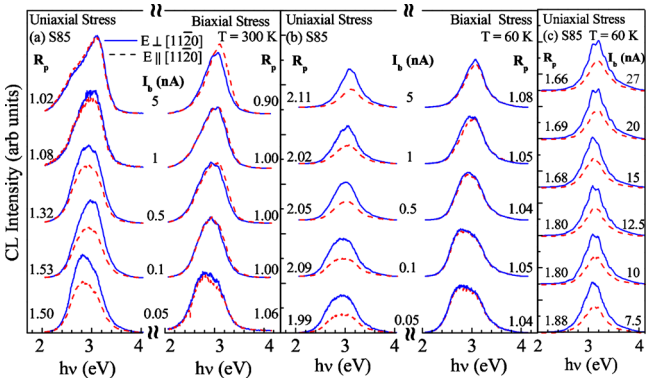

FIG. 2. (Color online) Stack plots of CL spectra of sample S85 acquired with polarization detection orientations of $\mathbf{E}\perp[11\bar{2}0]$ and $\mathbf{E}\parallel[11\bar{2}0]$ (perpendicular and parallel to a microcrack direction) for *e*-beam currents, I_b, ranging from 50 pA to 27 nA. The CL spectra were acquired with the *e*-beam focused in regions of pure uniaxial tensile stress and pure biaxial tensile stress, which were located at distances, Δx, of 0.5 μm and 5 μm, respectively, from the microcrack. CL spectra are shown for $T=300$ K and $T=60$ K. The polarization anisotropy ratio, $R_p=I_\perp/I_\parallel$, is indicated for each set of CL spectra acquired with *e*-beam currents, as shown.

the temperature decreases from 300 to 60 K. For sample S40, the polarization anisotropy is reduced in comparison to S85, but the trend is similar in the region of pure uniaxial stress as the maximum value of R_p increases from ~1.3 to 1.7 as the temperature decreases from 300 to 60 K, as shown in Fig. 3. For the region where biaxial stress is predominant ($\Delta x=5$ μm), R_p does not deviate far from 1 for both samples. The excitation dependent results for the polarization anisotropy ratio are summarized in Fig. 4, which show R_p as a function of I_b for temperatures of 60 and 300 K. Both experiment and theory are shown for comparison in Figs. 4(a) and 4(b). Of particular relevance is the large excitation dependence of R_p that is observed for temperatures of 300 K and yet noticeably diminished in the measurements at $T=60$ K for S85 and S40. For S85 at $T=300$ K, R_p is observed to decrease from ~1.5 to 1.0 nearly linearly with log

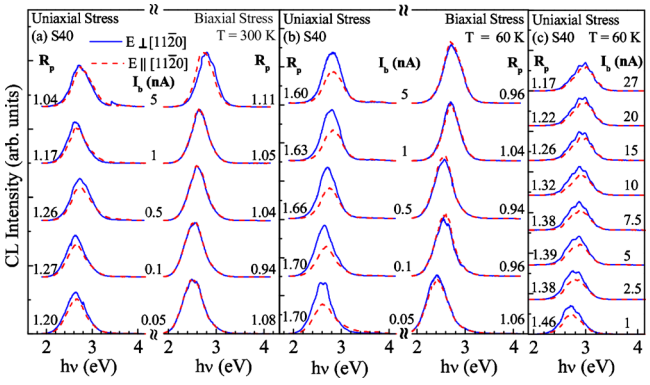

FIG. 3. (Color online) Stack plots of CL spectra of sample S40 acquired with polarization detection orientations of $\mathbf{E}\perp[11\bar{2}0]$ and $\mathbf{E}\parallel[11\bar{2}0]$ (perpendicular and parallel to a microcrack direction) for *e*-beam currents, I_b, ranging from 50 pA to 27 nA. The CL spectra were acquired with the *e*-beam focused in regions of pure uniaxial tensile stress and pure biaxial tensile stress, which were located at distances, Δx, of 0.5 μm and 5 μm, respectively, from the microcrack. CL spectra are shown for $T=300$ K and $T=60$ K. The polarization anisotropy ratio, $R_p=I_\perp/I_\parallel$, is indicated for each set of CL spectra acquired with *e*-beam currents, as shown.

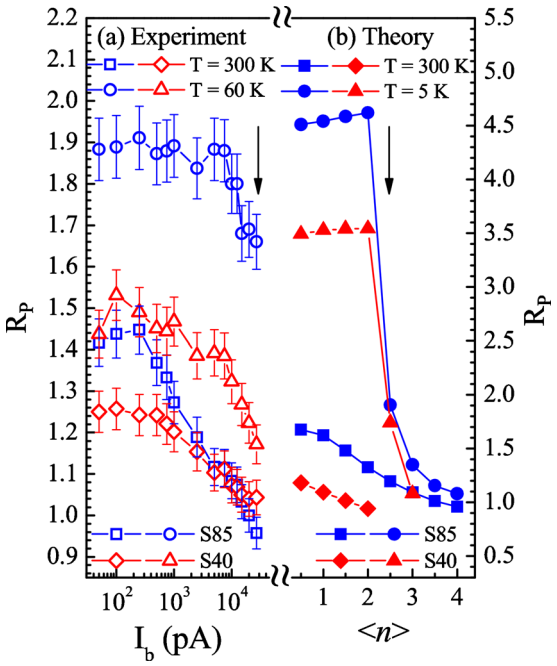

FIG. 4. (Color online) The experimental polarization anisotropy ratio, $R_p = I_\perp / I_\parallel$, vs I_b for for samples S85 and S40 at temperatures of 60 and 300 K in (a) and the calculated R_p vs $\langle n \rangle$ in (b). The calculations were performed self-consistently for uniaxial stress values of $\sigma_{yy}=30$ kbar for S85 and $\sigma_{yy}=20$ kbar for S40. The downward arrows indicate the locations of steps that occurred in R_p upon an increasing excitation at low temperatures for both the experimental data and calculations.

I_b as the *e*-beam current increases from 50 pA to 5 nA, while $R_p \approx 1.9$ and nearly constant over the same range of excitation for $T=60$ K. For larger beam currents approaching 27 nA at $T=60$ K, the values of R_p begin to decrease appreciably toward ~1.7 and 1.2 for S85 and S40, respectively. Thus, thermal energy at room temperature is observed to play an important role in the behavior of R_p for larger excitation conditions. Such a dependence on the excitation and temperature will be explained in the context of the thermal excitation of holes into higher energy QD hole states possessing partially orthogonal *p*-orbital characters in the discussion on theoretical modeling in Sec. IV D. As expected, for the regions of biaxial stress, R_p remains approximately 1 and independent of temperature and excitation, due to the biaxial symmetry.

B. Excitation dependence of the CL peak energies

The peaks of the polarized CL spectra for both samples are observed to sensitively depend on the excitation conditions and show a blueshift in both the biaxially and uniaxially stressed regions as I_b increases from 50 pA to 10 nA, as shown in Figs. 2 and 3. Time-resolved CL was carried out to measure the initial decay time, τ, as a function of I_b for each sample. Transients for the CL decay are shown in Fig. 5. The transients are observed to deviate from a simple single exponential behavior (i.e., a linear dependence in the semi-log plot) as I_b increases from 0.1 to 10 nA. The presence of slower decay components in the CL transients for higher I_b is a result of a partial screening of the polarization field in the GaN QDs during the initial part of the decay. This is a well-known effect attributed to carrier filling in the QD in which the quantum confined Stark effect leads to an electric field dependent *e-h* oscillator strength.[5] As the excitation density of the pulsed *e*-beam increases for large I_b, the initial larger screening of the field leads to an increased *e-h* oscillator strength and smaller decay time τ during the beginning of the decay transient. As the decay proceeds within a transient, the average screening gradually decreases, leading to a larger field, smaller oscillator strength and larger τ near the end of the transient. Thus, in order to obtain the carrier lifetime for a given steady state *e*-beam injection current, we utilize a linear fit to the initial portion of the transient resulting from a pulsed excitation at the same I_b used for steady-state excitation, as shown in Fig. 5. We have employed a standard approach that determines the relationship between the average *e-h* occupancy in the QD, $\langle n \rangle$, and the electron beam current, I_b.[27] In Fig. 6, we show the measured lifetime and $\langle n \rangle$ as a function of I_b for S85 and S40.

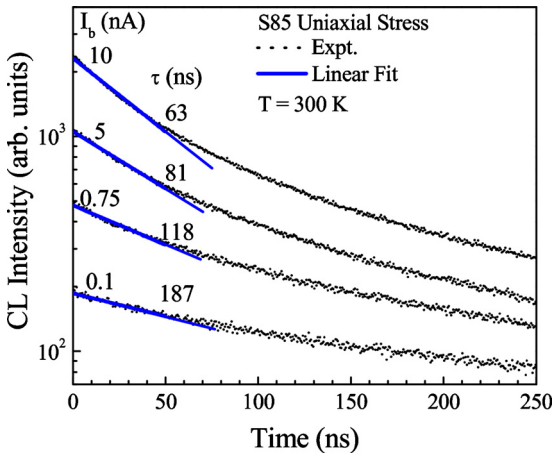

FIG. 5. (Color online) CL decay transients of sample S85 for various I_b. Lines shown tangent to the decay curves represent fits to the initial decay whose slopes yielded the decay times, τ, as shown. The measurements were performed in a region of uniaxial stress.

C. Modeling of the excitation-dependent QD electronic states and optical transitions

In order to develop a theoretical model for our luminescence data, evaluate the screening of the electric field in the QDs, and calculate the excitation dependence of the polarized CL spectra and anisotropy ratio, R_p, we have extended the multiband $\mathbf{k}\cdot\mathbf{p}$ and single band effective mass treatment for the occupation of multielectron and multihole states. Self-consistent calculations of the Schrödinger and Poisson equations using the 6×6 $\mathbf{k}\cdot\mathbf{p}$ and effective mass methods for the calculation of the *e-h* wave functions in the Hartree approximation were performed. The primary multicarrier correction to the energy levels results from the carrier-induced screening of the electric field in the QD which is caused by piezoelectric and pyroelectric polarization.

We calculate the electron and hole wave functions and energy levels while taking into account the modifications of the potential profile caused by the accumulation of carriers in the QDs. The modeling procedure is summarized with a flow chart in Fig. 7 which describes the procedure and order of

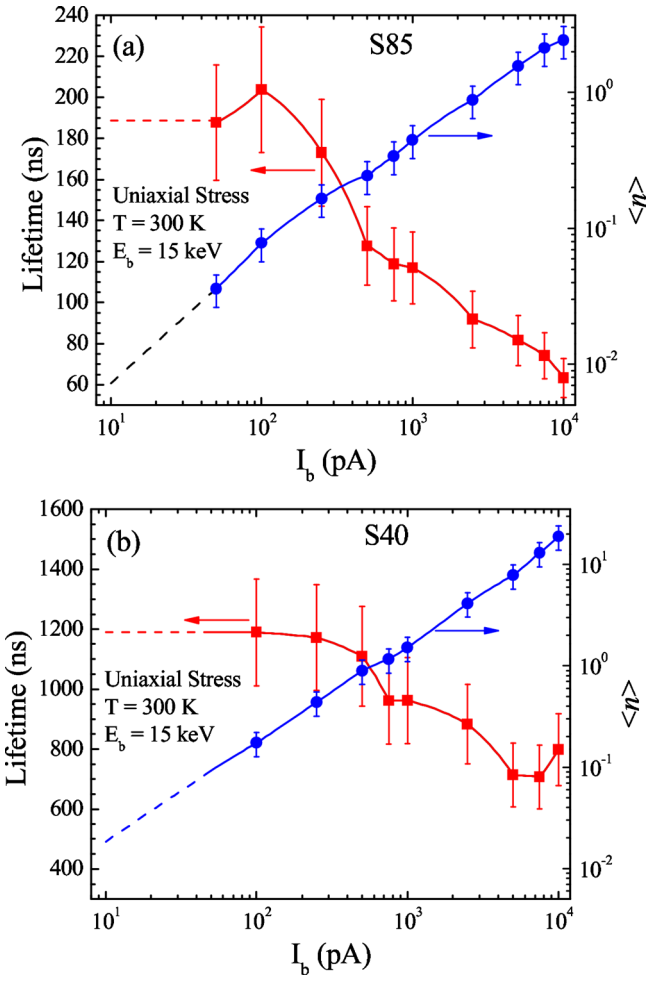

FIG. 6. (Color online) The measured lifetime, τ, and average occupation number, $\langle n\rangle$, for various e-beam injection currents, I_b, for samples S85 (a) and S40 (b) in regions of uniaxial stress. The relation described in Ref. 27 was used to connect $\langle n\rangle$ with I_b. Dashed lines represent extrapolated values for τ and $\langle n\rangle$.

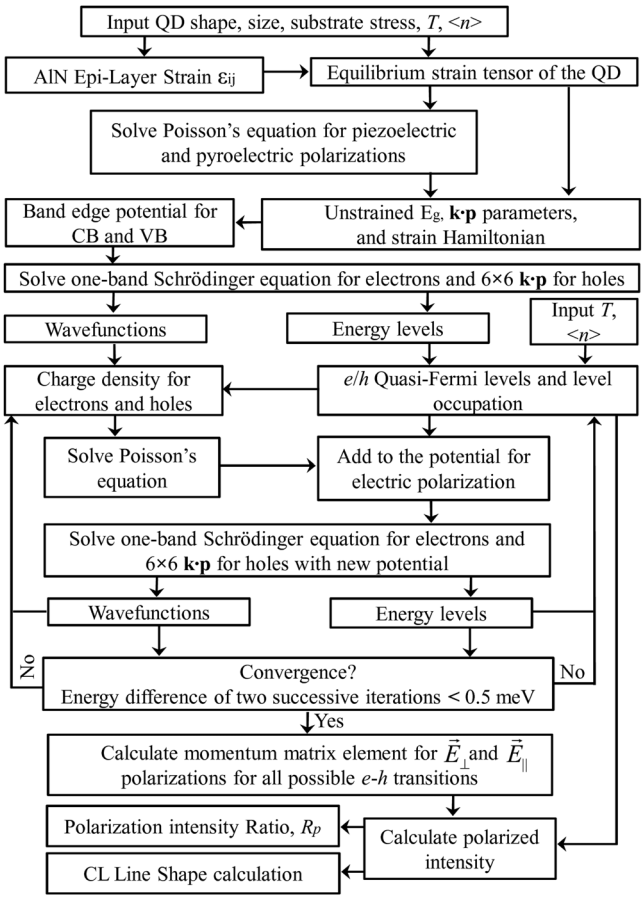

FIG. 7. Flow chart illustrating the details of the model calculations of the excitation dependent eigenstates and quasi-Fermi levels for the wurtzite GaN/AlN QD structures of S40 and S85. The model involves self-consistent solutions of the nonlinear Poisson-Schrödinger equation using the single band effective mass and the 6×6 $\mathbf{k}\cdot\mathbf{p}$ methods for the electron and hole eigenstates, respectively.

our self-consistent approach for solving the nonlinear Poisson-Schrödinger equation. The calculations for the wurtzite GaN QD system include the effects of strain, thermal stress, the microcrack-induced stress perturbation, deformation potentials, band offsets, and piezoelectric and spontaneous polarization fields to obtain the excitation-dependent eigenstates, electron and hole quasi-Fermi levels (φ_e and φ_h), and carrier occupation distribution among the QD electron and hole eigenstates. Solutions to the 6×6 $\mathbf{k}\cdot\mathbf{p}$ and effective mass Hamiltonians were obtained self-consistently. First, trial solutions of the e-h wave functions, ψ_i^e and ψ_j^h, and energies, E_i^e and E_j^h, for a given e-h occupation number $\langle n\rangle$ were obtained in the usual manner by first obtaining solutions without the Hartree correction potential, $V_H(\vec{r})$. Following the usual $\mathbf{k}\cdot\mathbf{p}$ formalism, the electron and hole wave functions are expressed as

$$|\psi_i^e\rangle = \sum_{k=1}^{2} F_{ei,k}^*(\vec{r})|k\rangle \quad \text{and} \quad |\psi_j^h\rangle = \sum_{l=1}^{6} F_{hj,l}^*(\vec{r})|l\rangle, \tag{1}$$

in which the Bloch part of the electron wave function, $|\psi_i^e\rangle$, is represented by two basis s-like states $|S\uparrow\rangle$ and $|S\downarrow\rangle$ and denoted by $|k\rangle$. The Bloch parts of the hole wave functions, $|\psi_j^h\rangle$, are represented by the six basis p-like functions, $|l\rangle$, in the following representation: $|x\uparrow\rangle, |y\uparrow\rangle, |z\uparrow\rangle, |x\downarrow\rangle, |y\downarrow\rangle$ and $|z\downarrow\rangle$, where coordinates x, y, and z refer to the $[1\bar{1}00]$, $[11\bar{2}0]$, and $[0001]$ crystallographic directions. For the hole state j, $F_{hj,l}(\vec{r})$ are the six hole envelope functions that are obtained from the 3D 6×6 $\mathbf{k}\cdot\mathbf{p}$ method and $F_{ei,k}(\vec{r})$ are the two electron envelope functions for the electron state i obtained from the 3D single effective mass calculation. The next step is the calculation of the electron and hole quasi-Fermi levels, φ_e and φ_h, for a given steady-state e-h pair occupation number, $\langle n\rangle$. From the discrete delta-function nature of the zero-dimensional QD density of states (DOS) and by invoking charge neutrality requirements during e-h excitation at a temperature T, φ_e, and φ_h are obtained from solutions to

$$\langle n\rangle = \sum_{i=1}^{N} f(E_i^e - \varphi_e) = \sum_{j=1}^{N} f(\varphi_h - E_j^h), \tag{2}$$

where $f(E)$ is the Fermi–Dirac function for electrons and holes, N is the largest state number that was used in the calculations, and electron and hole state occupancy is given individually by $n_i^e = f(E_i^e - \varphi_e)$ and $n_j^h = f(\varphi_h - E_j^h)$, respectively. Electron and hole spin degeneracy was also taken into

account in the calculations by assigning separate state numbers, i and j, to each set of degenerate time-reversal conjugate states. The next step is the calculation of the excess carrier charge density for the electrons and holes which depend on the quasi-Fermi levels and temperature according to

$$\rho_e(\vec{r}) = -e\sum_{i=1}^{N} f(E_i^{(e)} - \varphi_e)|\psi_i^e(\vec{r})|^2 \quad \text{and}$$

$$\rho_h(\vec{r}) = e\sum_{j=1}^{N} f(\varphi_h - E_j^{(h)})|\psi_j^h(\vec{r})|^2. \tag{3}$$

The Hartree contribution to the potential, $V_H(r)$, is then readily calculated from Poisson's equation as follows:

$$\vec{\nabla}[\varepsilon_r(\vec{r})\vec{\nabla}V_H(\vec{r})] = -\frac{1}{\varepsilon_0}[\rho_e(\vec{r}) + \rho_h(\vec{r})]. \tag{4}$$

The Hartree contribution is then added to the potential for charge polarization and the GaN/AlN band edge profiles, thereby enabling a series of iterative cycles involving the calculation of ψ_i^e, ψ_j^h, E_i^e, E_j^h, φ_e, and φ_h for a given temperature, T, and steady-state e-h occupation number, $\langle n\rangle$. We have set the convergence conditions such that successive iterations must differ by less than 0.5 meV in the electron and hole energies.

The integrated intensity of polarized luminescence is determined by the carrier occupation in the QD and the electron-hole wave function overlap according to

$$I_{\perp,\parallel} = \sum_{i,j} n_i^e n_j^h |M_{\perp,\parallel}^{(i,j)}(n_i^e, n_j^h)|^2,$$

where

$$M_{\perp,\parallel}^{(i,j)}(n_i^e, n_j^h) = \sum_{k=1}^{2}\sum_{l=1}^{6}\int d^3r F_{ei,k}^{*}(\vec{r})F_{hj,l}(\vec{r})\langle k|\hat{e}_{\perp,\parallel}\cdot\frac{\hbar}{i}\vec{\nabla}|l\rangle. \tag{5}$$

The unit electric field polarization vectors, $\hat{e}_{\perp,\parallel}$, represent polarizations that are perpendicular or parallel to the $[11\bar{2}0]$ microcrack directions, which we have defined as the y-axis direction in our coordinate system. The polarization anisotropy ratio, R_p, is then calculated from Eq. (5) as

$$R_p = \frac{I_\perp}{I_\parallel} = \frac{\Sigma_{i,j} n_i^e n_j^h |M_\perp^{(i,j)}(n_i^e, n_j^h)|^2}{\Sigma_{i,j} n_i^e n_j^h |M_\parallel^{(i,j)}(n_i^e, n_j^h)|^2}. \tag{6}$$

It is apparent from Eqs. (1) and (5) that the relative weights of the p_x and p_y orbitals, as determined by the relative values of the six hole envelope functions, $F_{hj,l}(\vec{r})$, will have an appreciable effect on the polarization anisotropy ratio R_p

We have calculated self-consistently the spectrum of electron and hole states using our self-consistent 6×6 $\mathbf{k}\cdot\mathbf{p}$ method. The energies of the electron and hole states, E_i^e and E_j^h, are shown as a function of the average occupation number $\langle n\rangle$ in Fig. 8 for S85 subject to a uniaxial stress of 30 kbar. As expected, the spectrum of hole states shifts downwards in energy with an average rate of ~15 meV and 9 meV, respectively, for S85 and S40, per addition of an e-h pair due to the partial screening of the electric field in the QD. A similar upward shift of ~8 meV and 5 meV, per e-h pair for electron levels also occurs, respectively, for S85 and S40, resulting in a net shift in the transition energy E_x that is ~23 meV and 14 meV per e-h pair, which is similar to changes observed in previous CL measurements.[28] These energy shifts are obtained by averaging over the values obtained for $\langle n\rangle$ ranging from 0.5 to 4 and 0.5 to 2 for S85 and S40, respectively. We note that differences in the average energy shift between the electron and hole states are due to differences in confinement and localization for both particles. We also note that the single band effective mass nature of the Schrödinger equation for the electrons and an approximately in-pane radially symmetric potential leads to well-defined s-, p-, and d-orbital symmetries and near-degeneracies, which are denoted by the groups of state numbers $\{i\}$ that are {1,2}, {3–6}, and {7–12}, as observed in Fig. 8(a).[29,30]

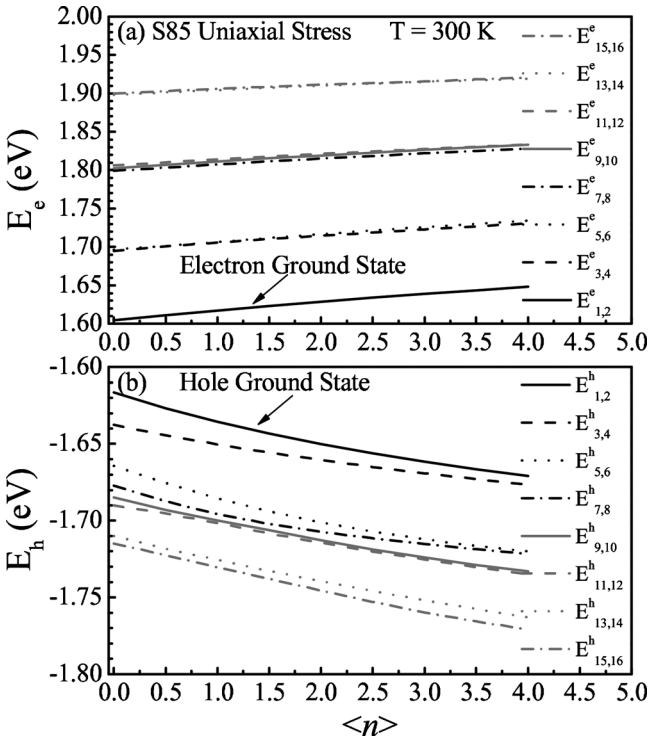

FIG. 8. The calculated electron (a) and hole (b) energy levels vs state occupancy $\langle n\rangle$ for the structure of S85 for the first eight e/h energy levels for T=300 K. The calculations were performed for the case of uniaxial stress with σ_{yy}=30 kbar. The collective upward and downward shifts in energy for the electron and hole states, respectively, are due to the screening of the QD electric field caused by filling of the electron and hole states through the state occupancy $\langle n\rangle$. The calculations were performed self-consistently and carriers were arranged among the states according to Fermi–Dirac statistics.

As the primary cause of the energy shifts is the Hartree term in the electrostatic potential, it is worth examining aspects of the calculation that lead to a partial screening of the [0001]-oriented polarization field of the QD, as shown in Fig. 9 for S85. Calculations were performed for the structures of S40 and S85 subject to uniaxial stresses of 20 and 30 kbar, respectively, along the direction of the $[11\bar{2}0]$-oriented microcrack. One-dimensional (1D) representations of the charge densities, $\rho_{e,h}(z)$, in which the charge densities are averaged over the x-y plane, are shown in Fig. 9 for S85. The charge density for the holes is shown inverted in Fig. 9(b).

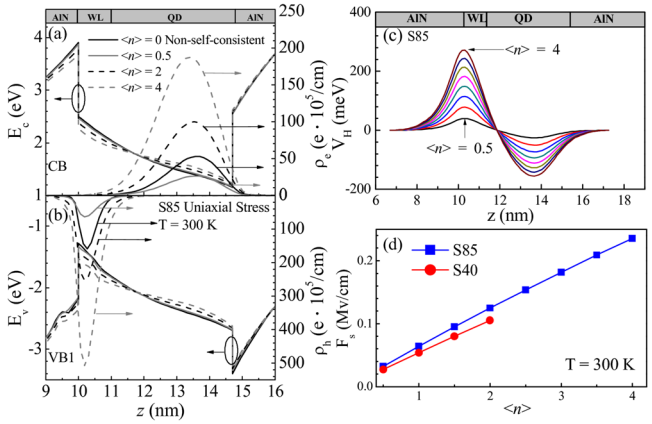

FIG. 9. (Color online) Self-consistent calculations of the conduction and valence band edge profiles along a line through the center of the QD and parallel to [0001] (i.e., the z-axis direction) for the structure of S85 in (a) and (b). The charge density for the electrons and holes, $\rho_{e,h}(z)$, integrated over the x-y plane is also shown interposed on the band-edge diagrams in (a) and (b), illustrating the strong localization in the wetting layer (WL) for holes and near the top of the QD for electrons. The calculations are shown for various e-h state occupancy $\langle n\rangle$ ranging from 0 to 4. Panel (c) shows the Hartree potential, $V_H(z)$, along the [0001] direction through the QD center for various $\langle n\rangle$ in the structure of S85. The average screening field, F_s, by which the total field is reduced, is shown in (d) for various $\langle n\rangle$ for both S40 and S85.

The charge densities are further shown overlayed on the 1D cross-section of the excitation-dependent band profiles for the conduction and valence band edges. As the occupation number $\langle n\rangle$ increases, the calculations show the expected screening of the band-edge potential and reduction in the average electric field along the [0001] QD axis. The reduced field leads to a broadening and shift in the centers of gravity for $\rho_{e,h}$ (z), which are both toward the center of the QD, consistent again with the expected increase in the e-h oscillator strengths for increasing excitation conditions. The Hartree term in the potential, $V_H(z)$, for a line along [0001] through the QD center, is also shown in Fig. 9(c) for various $\langle n\rangle$. The calculated average screening fields, F_s, along [0001] for both the S85 and S40 structures are shown in Fig. 9(d) as a function of $\langle n\rangle$. These values are consistent with previous studies showing carrier induced screening in GaN/AlN QDs.[5,28] The screening fields increase approximately linearly with $\langle n\rangle$, but exhibit small differences in slopes between the S85 and S40 structures. Such differences are attributed to differences in the S85 and S40 QD volumes. As the volume of S40 is ~60% larger than that of S85, a larger lateral confinement of the charges in the x-y plane for the S85 QD structure is expected to lead to a slightly larger F_s for a given $\langle n\rangle$ in S85, as observed in Fig. 9(d).

We have further calculated the excitation dependence of the CL spectra in order to compare with the measured energy shifts and polarization anisotropy. The CL spectra are modeled according to

$$I(h\nu) = \sum_{i,j} |M_{ij}|^2 f(E_i^{(e)} - \phi_e) f(\phi_h - E_i^{(h)}) \delta(h\nu - E_i^{(e)} - E_i^{(h)}), \quad (7)$$

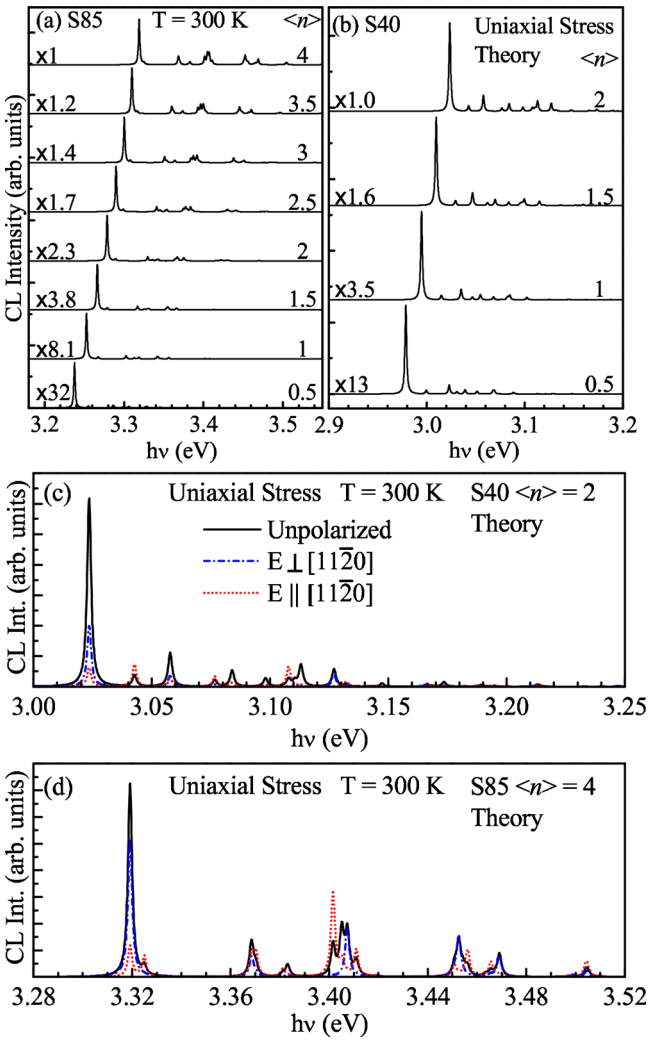

FIG. 10. (Color online) Calculated nonpolarized CL spectra for various $\langle n\rangle$ for the QD structures of S85 (a) and S40 (b). The calculations are for single QDs in the Hartree approximation for the screening of the polarization field. Calculations of the polarized CL spectra for S40 and S85 for $\langle n\rangle$=2 and $\langle n\rangle$=4 are shown in (c) and (d), respectively.

where M_{ij} is the momentum matrix element, the Dirac δ-function represents the electron and hole joint DOS, and $h\nu$ is the emitted photon energy. The excitation-dependent momentum matrix element, M_{ij}, is of the form expressed in Eq. (5) for polarized spectra with the electric field parallel or perpendicular to the microcracks or its square can be calculated by averaging over all three Cartesian directions, i.e., $|M_{ij}|^2 = (|M_{\perp}^{(i,j)}|^2 + |M_{\parallel}^{(i,j)}|^2 + |M_z^{(i,j)}|^2)/3$, for nonpolarized CL spectra. In either case, M_{ij} is calculated from the wave functions resulting from the self-consistent calculations. We approximate the broadening of the Dirac δ-functions with a Lorentizan function with homogenous width of 1 meV. The calculated nonpolarized CL spectra for a single QD subject to the uniaxial stress configuration at T=300 K are shown in Figs. 10(a) and 10(b) for the structures of S85 and S40 with various e-h occupation numbers $\langle n\rangle$. Gradual shifts in the various excitonic transitions toward higher energy due to screening of the field along with an increased participation of higher energy transitions are observed with increasing $\langle n\rangle$. Figures 10(c) and 10(d) show cases for calculated polarized

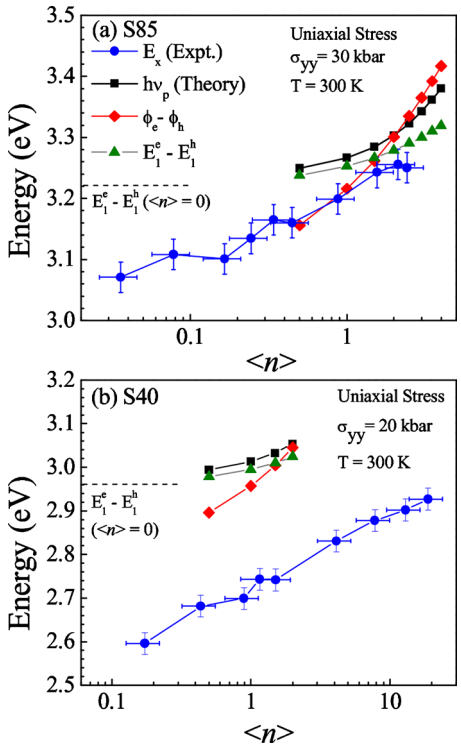

FIG. 11. (Color online) The measured CL peak QD transition energy (E_x), the calculated ground-state transition energy ($E_1^e - E_1^h$), the calculated peak energy position of the ensemble-broadened CL spectra ($h\nu_p$), and the calculated difference in the QD electron and hole quasi-Fermi levels ($\varphi_e - \varphi_h$) as a function of average state occupancy $\langle n \rangle$ for the structures of S85 (a) and S40 (b) subject to uniaxial stress and for $T=300$ K. The non-self-consistent calculation (i.e., $\langle n \rangle = 0$) for the ground-state transition energy ($E_1^e - E_1^h$) is shown with the horizontal dashed line for comparison. The relation between $\langle n \rangle$ and I_b is shown in Fig. 6.

CL spectra of a single QD under occupations of $\langle n \rangle = 2$ and $\langle n \rangle = 4$ for S40 and S85, respectively. Although the ground state transition is polarized as expected, a reversal in the anisotropy is observed for some higher energy transitions, leading to the decrease in the integrated R_p as $\langle n \rangle$ gradually increases in accordance with Fig. 4(b). In order to account for the inhomogeneous broadening of the QD ensemble in our samples, the intensity function $I(h\nu)$ is convoluted with a Gaussian which has a width β, and so the broadened calculated nonpolarized and polarized CL spectra are as follows:

$$L(h\nu) = \int_0^\infty d(h\nu') I(h\nu') \exp\left(-\frac{(h\nu - h\nu')^2}{\beta^2}\right). \quad (8)$$

We have used $\beta = 200$ meV, consistent with the observed experimental widths from the narrowest CL spectra of the QD ensembles. The energy shifts in the peak positions for the experimental and calculated spectra are observed to be in agreement, when considering the data of Fig. 6 which shows the relationship between I_b and $\langle n \rangle$.

In order to better facilitate a comparison with the experimental and calculated results, we show graphs of the experimental CL peak energy positions versus $\langle n \rangle$ and the results for the self-consistent calculations for varying excitation conditions in Fig. 11 for both S85 and S40. The calculated ground-state transition energy ($E_1^e - E_1^h$), difference in quasi-Fermi levels ($\varphi_e - \varphi_h$), and the calculated peak positions, $h\nu_p$, of $L(h\nu)$, obtained from Eq. (8), as a function of $\langle n \rangle$ at $T = 300$ K are shown in Fig. 11. As the quasi-Fermi levels represents the approximate energy positions of the highest electron and hole levels that participate in excitonic transition, their difference should then account for changes in these energy states due to the screening of the polarization field of the QD. Changes in $\varphi_e - \varphi_h$ with $\langle n \rangle$ should also reflect the energy shifts in E_x, associated with changes in the e-beam current, I_b. For the most part, the slopes of the experimental E_x and the calculated peak positions $h\nu_p$ versus $\langle n \rangle$ are in approximate agreement for both samples. Deviations between experiment and theory, and some experimental fluctuations are attributed to a nonuniform filling of the QDs owing to inhomogeneities in the excitation volume of the e-beam and the subsequent diffusion of carriers before collection into the QDs. Moreover, we have not included the Coulomb energy corrections which should lower the calculated energies by ~90 meV for these GaN/AlN QD sizes and shapes.[31] Although the calculated values for the energies of S40 are blueshifted by ~200 meV relative to the experimental peak energies for S40, these results represent a reasonable agreement between experiment and theory when considering the absence of the Coulomb correction and the large full-width-at-half-maxima of ~650 meV and ~490 meV and for the CL spectral line shapes of the broadened QD ensembles for S85 and S40, respectively, as observed in Figs. 2 and 3.

D. Analysis of the excitation-dependence of the polarization anisotropy

Spatial variations in the optical polarization properties are attributed to the stress-dependent variations in the p_x and p_y, characters of the valence band edges and the ground state hole wave function. In Fig. 12, the effect of a variable external uniaxial stress ($\sigma_{xx}=0$) on the e/h isosurfaces are shown for the structure of S85 is shown with $\sigma_{yy}=0$ kbar, 2.5 kbar, 10 kbar, and 30 kbar in panels (a)–(d), respectively, for the non-self-consistent case of $\langle n \rangle = 0$. Isosurfaces of the ground-state hole e/h wave function (with $|\psi_{e,h}(\vec{r})|^2 = a_{e,h}|\psi_{\max}|^2$, where $|\psi_{\max}|^2$ is the maximum probability density of the wave function) for the S85 structure are shown with $a_e = 0.01$ and $a_h = 0.1$ so as to distinguish more easily between the two states. It is apparent that the s-like electron state retains its near cylindrical symmetry for all uniaxial stress values shown. However, the shape and direction of elongation of the hole isosurface changes in Fig. 12 as the value of σ_{yy} is increased toward its maximum value of 30 kbar which was used in our calculations. Similar results were observed for calculations for the structure of S40. Figures 12(e) and 12(f) show 3D plots of the e/h isosurfaces ($a_e = a_h = 0.1$) for S85 with a uniaxial stress ($\sigma_{yy}=30$ kbar and $\sigma_{xx}=0$) and a biaxial stress ($\sigma_{yy}=\sigma_{xx}=30$ kbar), respectively, illustrating the structure of the QD and spatial separation of the e/h wave functions along [0001]. Previously, we showed that a change from biaxial to uniaxial stress alters the admixture of p_x and p_y characters of the band edges and ground state hole wave function, changes the shape and direction of elongation of the hole isosurfaces, and accounts well for the subsequent

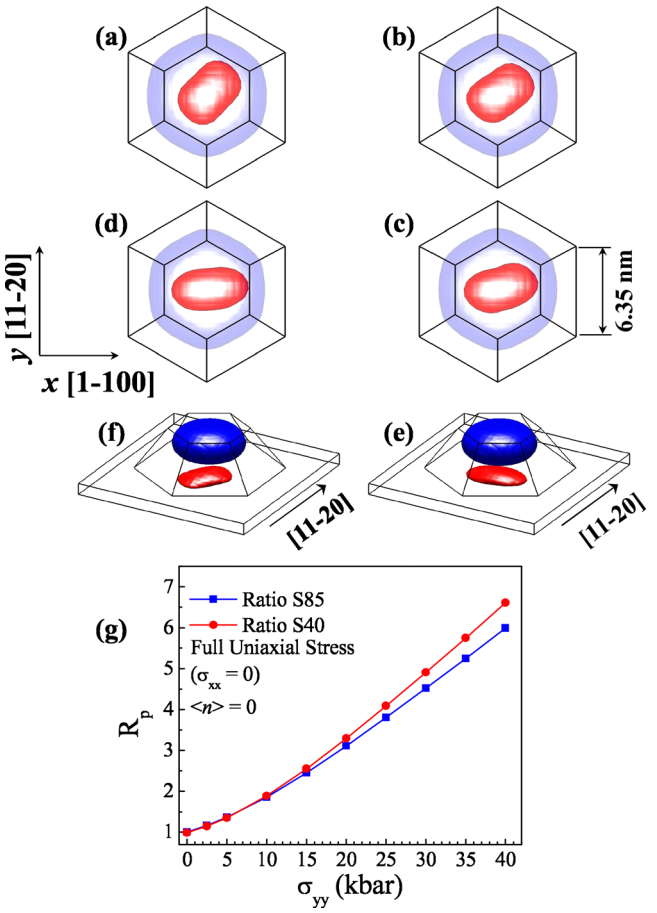

FIG. 12. (Color online) Isosurfaces of the ground state hole and electron wave functions for the structure of S85 for $\langle n\rangle=0$. Surfaces of constant probability density, $|\psi_h(\vec{r})|^2=0.1|\psi_{\max}|^2$ and $|\psi_e(\vec{r})|^2=0.01|\psi_{\max}|^2$ are plotted for uniaxial stress values of $\sigma_{yy}=0$ kbar, 2.5 kbar, 10 kbar, and 30 kbar in (a)–(d), respectively. Projections of the hexagonal base and apex of the pyramidal GaN QD are shown for each isosurface. The apparent variations in shade on the isosurfaces are due to a simulated reflection of light rays impinging on the surface from above. A 3D perspective of the QD structure and the electron and hole isosurfaces are shown in (e) and (f) for the structure S85 subject to in-plane uniaxial and biaxial stresses of 30 kbar, respectively. A plot of the calculated polarization anisotropy ratio, R_p, vs uniaxial stress, σ_{yy}, is shown in (g).

anisotropy in the ground state polarization dependent optical transitions and its spatial variation in the vicinity of the microcracks.[10] Thus, this same interpretation ought to apply for the case of a variable uniaxial stress. Indeed, a calculation of R_p versus σ_{yy} for the present case is shown for both S40 and S85 structures in Fig. 12(g), illustrating the connection between hole isosurface orientation, admixture of p_x and p_y characters, and the resulting R_p.

The striking temperature dependent behavior of R_p in Figs. 2–4 suggest thermal excitation to higher lying hole states plays an important role in reducing R_p for higher excitation conditions at room temperature. Since the energy spacing between confined electron states is ~4–5 times greater than the spacing for hole states, which have spacings typically ranging from 10–20 meV, we hypothesize that the thermal excitation for holes near $T=300$ K will have an appreciable effect on the distribution of hole occupancy, particularly for high excitation conditions (i.e., $\langle n\rangle > \sim 1$).

It is possible to observe the position and stress dependent character of the wave function by projecting the two

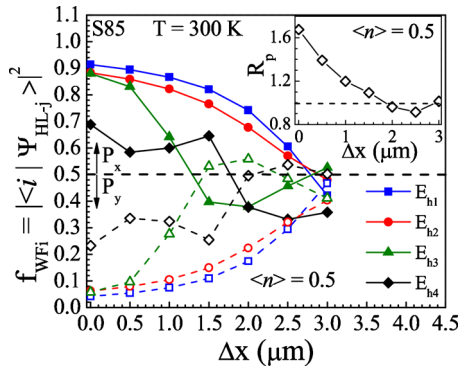

FIG. 13. (Color online) The relative p_x and p_y orbital characters of the Bloch states, $f_{WFi}=|\langle i|\psi_h\rangle|^2$ where $i=x$ or y, shown as a function of position, Δx, relative to a microcrack for the first four hole states for $\langle n\rangle=0.5$. The calculations were performed self-consistently. The inset shows the calculated R_p vs Δx, where $\Delta x=0$ and 3 μm represent positions of pure uniaxial and biaxial stresses of 30 kbar.

Bloch states with like spin, $|x\rangle$ and $|y\rangle$ onto the hole wave function by calculating $f_{WFi}=|\langle i|\psi_h\rangle|^2$ where $i=x$ or y. We note that y is referenced as the $[11\bar{2}0]$ microcrack direction in the calculations. We show f_{WFi} for the lowest four hole states as a function of distance, Δx, from a microcrack in Fig. 13. The relative p_x-orbital character of the Bloch states, f_{WFi}, reduces significantly for higher energy hole states (i.e., for $j\geq 2$) for uniaxial stress ($\Delta x=0$) and approaches ~0.5 for biaxial stress ($\Delta x=3$ μm). The present case in Fig. 13 is illustrated for $\langle n\rangle=0.5$, but also shows similar results for larger $\langle n\rangle$. The case of $\langle n\rangle=0.5$ is important since it is a self-consistent calculation for E_x that reflects the lowest energy excitonic transition in Slater's ground state transition and should therefore most closely represent the experimental ground state e-h transition for low excitation conditions.[32] The inset of Fig. 13 further shows the calculation of R_p versus Δx, confirming that R_p reduces from ~1.7 to ~1 in transitioning from uniaxial to biaxial stress.

Thus, we expect that the polarization anisotropy ratio R_p will decrease for optical transitions that involve increasingly higher energy hole states, as obtained by increasing e-h occupation numbers, $\langle n\rangle$, or an enhanced thermal excitation to higher energy hole states for $T=300$ K. Using the spectrum of hole wave functions in S40 and S85 that were calculated self-consistently, we have calculated R_p at high and low temperatures (300 and 5 K) using Eq. (6) by taking into account the occupation of the excited holes using Fermi–Dirac statistics in a fully self-consistent fashion involving separate electron and hole occupation numbers, n_i^e and n_j^h. Using this method, the calculated R_p versus $\langle n\rangle$ is shown for both structures in Fig. 4(b) at $T=5$ and 300 K, in order to consider the extreme temperature limits involved with thermal excitation of the hole states. The results agree qualitatively with the experimental polarized CL results for R_p, as shown in Fig. 4(a). For low temperatures, it is apparent that a minimal thermal excitation of the hole states results in an R_p that is roughly independent of excitation until the first electron and hole levels are doubly occupied. Upon increasing the excitation ($I_b > \sim 12$ nA), a sudden decrease in R_p is observed at low temperatures where a step is observed (downward ar-

rows) for both samples in Fig. 4(a). Such a decrease in R_p at higher excitations is consistent with the participation of higher energy hole states whose relative p_x-orbital character of the Bloch states, f_{WFi}, also decreases, as observed in Fig. 13. In comparison, R_p decreases gradually and nearly linearly as a function of $\langle n \rangle$ at $T=300$ K, as observed in Fig. 4 for both the experiment and calculations for S40 and S85. Thus, we attribute carrier filling and a thermal excitation of holes into higher energy hole states during excitation to account for a nearly linear decrease in R_p with $\langle n \rangle$ at $T=300$ K, while almost no thermal excitation of holes occurs at the lowest temperatures in the calculations ($T=5$ K).

V. CONCLUSION

In this work, GaN/AlN self-assembled QDs were grown by the Stranski–Krastanov method on a Si(111) substrate using MBE. During the subsequent cooling from growth temperatures, microcracks formed parallel to the interface and mainly along the $\langle 11\bar{2}0 \rangle$ directions. We demonstrated that these defects serve as excellent stressors, providing limited regions of in-plane uniaxial stress which can be exploited to perturb the electronic states of the QDs. The excitonic luminescence of QDs with a uniaxial stress perturbation exhibits an in-plane linear polarization anisotropy. Localized CL spectroscopy of the QDs exhibits emissions from both the ground and excited states, whose relative contributions depend on the level of excitation and temperature. We have studied these emissions using polarization-resolved CL for ensembles of QDs. The effects of screening of the polarization field in the QD and state-filling were studied experimentally with CL and theoretically with a 3D 6×6 $\mathbf{k}\cdot\mathbf{p}$ self-consistent calculation method for solving the Schrödinger and the Poisson equations. In the modeling, we examined occupation of the excited QD electron and hole states, determined the quasi-Fermi levels, and calculated the excitation and uniaxial stress dependence of the CL polarization anisotropy. Experimental results indicate that the CL polarization anisotropy ratio R_p vanishes at high temperatures with an increasing excitation of the QDs, while the anisotropy decreases more slowly with excitation at low temperatures. We attribute carrier filling and a thermal excitation of holes into higher energy hole states during excitation to account for a nearly linear decrease in the polarization anisotropy ratio, R_p, with $\langle n \rangle$ at $T=300$ K, while almost no thermal excitation of holes occurs at the lowest temperatures in the calculations ($T=5$ K). These results demonstrate the complex interplay between external stress, temperature, and excitation conditions on the polarization dependence of the excitonic luminescence from an ensemble of GaN/AlN self-assembled QDs.

[1]S. Tanaka, H. Hirayama, Y. Aoyagi, Y. Narukawa, Y. Kawakami, and S. Fujita, Appl. Phys. Lett. **71**, 1299 (1997).
[2]B. Damilano, N. Grandjean, F. Semond, J. Massies, and M. Leroux, Appl. Phys. Lett. **75**, 962 (1999).
[3]B. Damilano, N. Grandjean, J. Massies, and F. Semond, Appl. Surf. Sci. **164**, 241 (2000).
[4]A. D. Andreev and E. P. O'Reilly, Phys. Rev. B **62**, 15851 (2000).
[5]S. Kalliakos, T. Bretagnon, P. Lefebvre, T. Taliercio, B. Gil, N. Grandjean, B. Damilano, A. Dussaigne, and J. Massies, J. Appl. Phys. **96**, 180 (2004).
[6]V. Ranjan, G. Allan, C. Priester, and C. Delerue, Phys. Rev. B **68**, 115305 (2003).
[7]A. Dadgar, A. Strittmatter, J. Bläsing, M. Poschenrieder, O. Contreras, P. Veit, T. Riemann, F. Bertram, A. Reiher, A. Krtschil, A. Diez, T. Hempel, T. Finger, A. Kasic, M. Schubert, D. Bimberg, F. A. Ponce, J. Christen, and A. Krost, Phys. Status Solidi C **0**, 1583 (2003).
[8]D. Rudloff, T. Riemann, J. Christen, Q. K. K. Liu, A. Kaschner, A. Hoffmann, Ch. Thomsen, K. Vogeler, M. Diesselberg, S. Einfeldt, and D. Hommel, Appl. Phys. Lett. **82**, 367 (2003).
[9]G. Sarusi, O. Moshe, S. Khatsevich, D. H. Rich, and B. Damilano, Phys. Rev. B **75**, 075306 (2007).
[10]O. Moshe, D. H. Rich, B. Damilano, and J. Massies, Phys. Rev. B **77**, 155322 (2008).
[11]O. Moshe, D. H. Rich, B. Damilano and J. Massies, J. Vac. Sci. Technol. B **28**, C5E25 (2010).
[12]O. Moshe, D. H. Rich, B. Damilano, and J. Massies, Phys. Status Solidi C **6**, 1432 (2009).
[13]N. F. Gardner, J. C. Kim, J. J. Wierer, Y. C. Shen, and M. R. Krames, Appl. Phys. Lett. **86**, 111101 (2005).
[14]H. Masui, H. Yamada1, K. Iso, S. Nakamura, and S. P. DenBaars, J. Phys. D **41**, 225104 (2008).
[15]H. Masui, H. Yamada, K. Iso, J. S. Speck, S. Nakamura, and S. P. DenBaars, J. Soc. Inf. Disp. **16**, 571 (2008).
[16]Y. R. Wu, Y. Y. Lin, H. H. Huang, and J. Singh, J. Appl. Phys. **105**, 013117 (2009).
[17]J. Lee, H. N. Spector, and W. C. Chou, Phys. Status Solidi B **242**, 2846 (2005).
[18]U. Hohenester, R. D. Felice, and E. Molinari, Appl. Phys. Lett. **75**, 3449 (1999).
[19]B. Daudin, F. Widmann, G. Feuillet, Y. Samson, M. Arlery, and J. L. Rouviere, Phys. Rev. B **56**, R7069 (1997).
[20]M. Miyamura, K. Tachibana, and Y. Arakawa, Appl. Phys. Lett. **80**, 3937 (2002).
[21]H. T. Lin, D. H. Rich, A. Konkar, P. Chen, and A. Madhukar, J. Appl. Phys. **81**, 3186 (1997).
[22]K. H. Lee, J. H. Na, R. A. Taylor, S. N. Yi, S. Birner, Y. S. Park, C. M. Park, and T. W. Kang, Appl. Phys. Lett. **89**, 023103 (2006).
[23]V. A. Fonoberov and A. A. Balandin, J. Vac. Sci. Technol. B **22**, 2190 (2004).
[24]I. Vurgaftman and J. R. Meyer, J. Appl. Phys. **94**, 3675 (2003); I. Vurgaftman, J. R. Meyer, and L. R. Ram-Mohan, *ibid.* **89**, 5815 (2001).
[25]O. Ambacher, J. Majewski, C. Miskys, A. Link, M. Hermann, M. Eickhoff, M. Stutzmann, F. Bernardini, V. Fiorentini, V. Tilak, B. Schaff, and L. F. Eastman, J. Phys.: Condens. Matter **14**, 3399 (2002).
[26]D. P. Williams, A. D. Andreev, E. P. O'Reilly, and D. A. Faux, Phys. Rev. B **72**, 235318 (2005); D. P. Williams, A. D. Andreev, and E. P. O'Reilly, *ibid.* **73**, 241301 (2006).
[27]The average carrier density is represented by $\langle n \rangle = (I_b E_b \tau L_D)/(3eE_g V_{ex} A_D)$, where L_D is the spacing between the QD layers, A_D is the areal density of the QDs, and V_{ex} is the excitation volume of the $E_b=15$ keV electron beam. We have used $V_{ex}=2.1$ μm^3 for the present GaN/AlN material system.
[28]G. Salviati, F. Rossi, N. Armani, V. Grillo, O. Martinez, A. Vinattieri, B. Damilano, A. Matsuse, and N. Grandjean, J. Phys.: Condens. Matter **16**, S115 (2004).
[29]P. Tronc, V. P. Smirnov, and K. S. Zhuravlev, Phys. Status Solidi B **241**, 2938 (2004).
[30]See, e.g., O. Gywat, H. J. Krenner, and J. Berezovsky, *Spins in Optically Active Quantum Dots* (Wiley-VCH Verlag GmbH and CO. KgaA, Weinheim, 2010), pp. 24–27.
[31]V. A. Fonoberov and A. A. Balandin, J. Appl. Phys. **94**, 7178 (2003).
[32]J. C. Slater, Adv. Quantum Chem. **6**, 1 (1972).